CHEMISTRY OF MATERIALS
Cite This: Chem. Mater. 2019, 31, 5655−5662
Article
pubs.acs.org/cm

Controlling Anisotropy of Quantum-Confined $CsPbBr_3$ Nanocrystals by Combined Use of Equilibrium and Kinetic Anisotropy

Yitong Dong,[†,∥] Tian Qiao,[†,∥] Doyun Kim,[†] Daniel Rossi,[†] Sang Jung Ahn,[‡] and Dong Hee Son*[,†,§]

[†] Department of Chemistry, Texas A&M University, College Station, Texas 77843, United States
[‡] Korea Research Institute of Standards and Science, Daejeon 34113, Republic of Korea
[§] Center for Nanomedicine, Institute for Basic Science (IBS), Seoul 03722, Republic of Korea

* Supporting Information

ABSTRACT: Anisotropic semiconductor nanocrystals with controlled quantum confinement are important in many applications for the directionality of the flow of photons and charge carriers combined with the properties of confined exciton. Here, we report the strategy that introduces controlled morphological anisotropy with one- and two-dimensional confinements in $CsPbBr_3$ nanocrystals via the simultaneous use of thermodynamic equilibrium and kinetic anisotropy. In this approach, the halide equilibrium recently shown to control the size of zero-dimensional perovskite quantum dots under hot-injection condition is combined with the anisotropic growth kinetics that becomes more prominent at a lower temperature. Nanoribbons, nanowires, and nanoplatelets exhibiting well-defined confined exciton transition and high-emission polarization anisotropy were obtained at room temperature. While two seemingly incompatible modes of size control (equilibrium and kinetics) are combined, each mode controls the size in a different direction of the anisotropic perovskite nanocrystals, enabling the simultaneous control of confinement and morphological anisotropy.

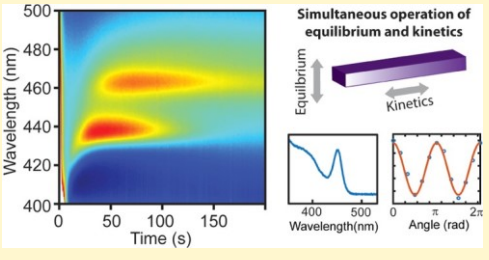

INTRODUCTION

Semiconductor nanocrystals with an anisotropic shape with one- and two-dimensional quantum confinements combine the properties of spatially confined exciton with the directionality of the optical[1−4] and transport properties[5−7] dictated by their anisotropic morphology and dimensionality. For this reason, much effort has been made in the last decades in developing the methods of controlling the size and anisotropic morphology,[8−12] which can add the ability to control the direction of the emission polarization or charge flow via orientational control of the nanocrystals in space. Often, the extrinsic means of inducing anisotropic growth is introduced for the synthesis of anisotropic nanocrystals, especially when the intrinsic anisotropy of the growth kinetics is weak. A common strategy is exploiting the difference of the ligand binding affinity on different facets that result in different growth rates in different directions.[10,11,13] The use of a seed that directs the growth in a particular direction has also been utilized to synthesize anisotropic structures such as nanowires.[14−17] Recently, efforts to create the anisotropic nanocrystals have been extended to the lead halide perovskites,[18−26] which exhibited superior functionality as the source of photons and charge carriers compared to many other semiconductor nanocrystals. Although the cube-shaped lead halide perovskite nanocrystals are commonly formed under typical hot-injection synthesis condition due to the near-cubic lattice symmetry,[27] several recent studies demonstrated the successful formation of anisotropic structures. In the case of cesium lead halide ($CsPbX_3$) nanocrystals, nanoplatelets (NPLs)[20,22,23,26] and nanowires (NWs)[25] have been synthesized by varying the surface-binding ligands or condition for the ligand binding and temperature. For instance, the concentration of the ligands,[25,26] the length of the tail group in the ligand,[20,22,25] and protonation/deprotonation equilibrium of the ligand[23,26] were varied in addition to the reaction temperature,[28] which are considered to modify the kinetic anisotropy. Similar methods were also used to synthesize the anisotropic nanocrystals of organometallic hybrid perovskites.[29−32] On the other hand, a wide range of synthesis conditions and the reactants in these studies also made it difficult to converge a

DOI: 10.1021/acs.chemmater.9b01515
Chem. Mater. 2019, 31, 5655−5662

systematic approach that can control the anisotropic morphology and size with a high-ensemble uniformity.

Here, we report a very different synthesis approach capable of creating one- and two-dimensional $CsPbBr_3$ nanocrystals exhibiting well-defined anisotropic and quantum-confined optical properties, which utilizes the thermodynamic equilibrium of halide and kinetic anisotropy simultaneously. Recently, we developed the method to control the size of cube-shaped $CsPbX_3$ quantum dots (QDs) (X = Cl, Br, I) in strongly confined regime by utilizing the thermodynamic equilibrium of halide between the QD lattice and solution medium through the law of mass action.[33] The size control in $CsPbX_3$ QDs via halide equilibrium was achieved under hotinjection condition by taking advantage of the highly labile

Received: April 16, 2019
Revised: July 8, 2019
Published: July 15, 2019

nature of halide ions in $CsPbX_3$ lattice and the size-dependent halide composition of $CsPbX_3$ QDs (higher halide content in the smaller QD). The smaller QDs were obtained at the higher halide concentration in the reactant, and the terminal size of the QDs was insensitive to the nucleation and growth kinetics, producing the QDs with very high ensemble uniformity. In this work, we combined the equilibrium-based size control shown to be highly effective in the synthesis of QDs with the roomtemperature reaction that promotes the anisotropic growth to produce the anisotropic $CsPbBr_3$ nanocrystals with controlled one- and two-dimensional quantum confinements. Unlike in the synthesis of QDs under hot-injection condition, where the halide equilibrium is the dominating mechanism for the isotropic size control, the room-temperature reaction provides a more favorable condition to utilize any existing kinetic anisotropy. Under the room-temperature reaction condition employed here, both the halide equilibrium and kinetic anisotropy appear to be in play, determining the size in different directions in different manners. Only the shortest dimension (thickness) that determines the band gap exhibited the behavior of the size control via halide equilibrium, i.e., varied with halide concentration independent of the reaction time. In contrast, the growth in the other directions exhibited a more typical behavior of kinetically controlled growth, i.e., increasing the length with increasing reaction time. Despite the complexity involving both the halide equilibrium and kinetic anisotropy, we could tune the anisotropic morphology of $CsPbBr_3$ nanocrystals by varying only the source and amount of excess halide at fixed reaction temperature. Using this approach, we produced $CsPbBr_3$ nanowires (NWs), nanoribbons (NRs), and nanoplatelets (NPLs) exhibiting strong optical anisotropy and spectrally narrow luminescence from tightly controlled quantum confinement. These nanocrystals are also readily purified via precipitation/resuspension cycles removing the remaining unreacted salts, which improved the stability under a moderately intense photoexcitation important for the photonic applications. One could further explore the approach combining the halide equilibrium and kinetic anisotropy to expand the capability to achieve a higher level of control over the anisotropic morphology and size in other metal halide perovskite systems.

RESULTS AND DISCUSSION

Since we utilize the halide equilibrium and kinetic anisotropy simultaneously to control the size and anisotropic morphology of $CsPbBr_3$ nanocrystals, the concentration of Br^- ($[Br^-]$) in the reactant mixture and the temperature are the two most important experimental variables. In this study, all of the reactions were performed at room temperature (23 °C), under which the anisotropic growth kinetics is more apparent than at hot-injection temperature favoring the formation of isotropic nanocubes, and only the condition controlling $[Br^-]$ was varied. The variation of $[Br^-]$ in a wide range, necessary to tune the morphology and size, was achieved using several divalent metal bromides (MBr_2, M = Co, Cu) as the source of excess halide. MBr_2 is chosen since it was demonstrated to be highly effective in controlling the size of $CsPbBr_3$ QDs via halide equilibrium without interference from M^{2+} when chosen appropriately (e.g., Zn and Co) in our recent study.[33] The composition and the concentration of the organic ligands that passivate the surface, also known to influence the growth kinetics and morphology,[20,22,23,25,26] were kept constant in this study to rule out the "ligand effect" in controlling the morphology and size.

A brief synthesis procedure is described below, and the details of the reaction conditions are in the Experimental Section. The precursor solution of Pb and Br was prepared by dissolving $PbBr_2$ and MBr_2 (M = Co, Cu) in a mixture of octadecene (ODE), oleylamine (OAm), and oleic acid (OA). The precursor solution of Cs was prepared by dissolving Cs_2CO_3 in a mixture of OA and ODE. The two precursor solutions were combined in a flask at room temperature. At this stage, the reactant mixture is not sufficiently reactive to form the nanocrystals or the smaller structures that can act as the seed for the growth such as the small clusters[28] or L_2PbBr_4 monolayer structure.[34] This is confirmed by the complete absence of the distinct absorption peak near 400 nm previously observed from the clusters and L_2PbBr_4 monolayer structure in the absorption spectrum of the precursor solutions (Figure S1). The reaction was initiated by adding a polar solvent (e.g., acetone) to the reactant mixture, where the sudden increase of the solvent polarity makes Br^- and other metal ions available for the reaction. Nanocrystals of different anisotropic morphology and size were obtained by varying the amount of $CoBr_2$ or $CuBr_2$ in the precursor solution and keeping all of the other reaction conditions identical. Among many MBr_2 that can potentially be used as the source of Br^-, $CoBr_2$ and $CuBr_2$ were chosen because of their relatively high solubility in the nonpolar

DOI: 10.1021/acs.chemmater.9b01515
Chem. Mater. 2019, 31, 5655−5662

solvent (mixture of ODE, OAm, and OA) at room temperature needed to vary [Br^-] in a wide range.

Figure 1 summarizes the synthesis of the anisotropic $CsPbBr_3$ nanocrystals with varying thickness (t), width (w), and length (l) in the form of nanoribbons (NRs, t < w < l), nanoplatelets (NPLs, t < w ≈ l), and nanowires (NWs, t = w < l). The top panel in Figure 1 illustrates the empirical correlation between the morphology of the anisotropic $CsPbBr_3$ nanocrystals and the identity and relative amount of MBr_2 used as the source of excess Br^-. In general, the morphology progressed from NWs to NRs and NPLs as [Br^-] increases in the reactant mixture. For a given morphology, thinner structures were obtained at the higher [Br^-]. For the synthesis of NWs, $CoBr_2$ was used as the source of excess Br^-. For the synthesis of NRs requiring higher [Br^-] than in the synthesis of NWs, $CuBr_2$ was used as the source of excess Br^-. Cu^{2+} ions can form a stable complex with a large number of Br^- ions in nonpolar solvents, which can achieve higher [Br^-] than other MBr_2 when acetone initiates the reaction. More detailed discussion on the function of $CuBr_2$ as the source of excess Br^- will be discussed later. For NPLs that require the highest [Br^-], a combination of $CuBr_2$ and $CoBr_2$ (or $ZnBr_2$) was used as the source of excess Br^-. To confirm the absence of a critical role of metal cations in determining the thickness, a control experiment was performed where a metal bromide is replaced with a halide-free metal salt such as metal stearate. The variation of the amount of metal stearate did not show any ability to tune the morphology or thickness of $CsPbBr_3$ nanocrystals in contrast to metal bromides, indicating the crucial role of Br^- in controlling the anisotropic morphology and size (Figure S2).

Figure 1a–e shows the absorption and photoluminescence (PL) spectra of $CsPbBr_3$ NRs, NPLs, and NWs, whose average dimensions are indicated in each panel. The corresponding TEM images are shown in Figure 1f–o. X-ray diffraction (XRD) patterns of these anisotropic nanocrystals are also provided in the Supporting Information (Figure S3). As stated

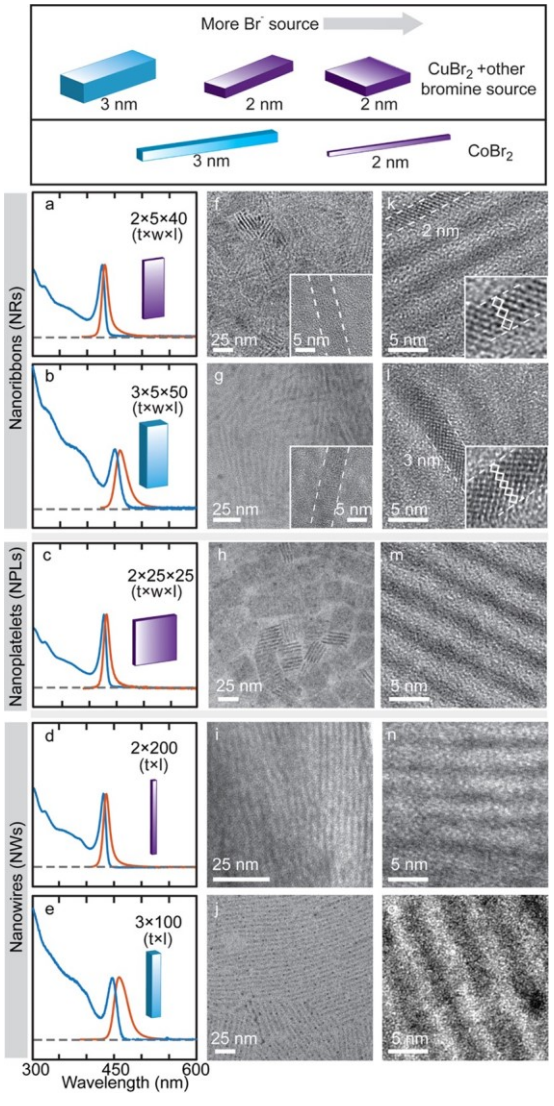

Figure 1. (a–e) Absorption (blue) and photoluminescence (PL) spectra (red) of NRs, NPLs, and NWs. The dimension of each nanocrystal is indicated in each panel. (f–j) Wide-view transmission electron microscopy (TEM) images of the nanocrystal corresponding to the optical spectra in (a)–(e). The insets in (f) and (g) show the NRs lying flat on the substrate, revealing the width different from the thickness. (k–o) TEM images at the higher magnification showing the thickness of each nanocrystal sample. The insets of (k) and (l) clearly show the number of $PbBr_6^{4-}$ octahedral units n = 3 and 5, respectively.

earlier, an interesting aspect of the synthesis method reported in this work is that only the shortest dimension (t) exhibits the pattern of size control via halide equilibrium, while the growth in other dimensions follows the more typical pattern of growth governed by the kinetics. In both NRs and NWs, the smaller t was obtained at higher [Br^-] as in the case of the hot-injection synthesis of $CsPbBr_3$ QDs, where the smaller QDs were obtained when [Br^-] is higher in the reactant mixture.[33] The independence of t on the reaction time after the terminal t is reached in NRs and NWs is also the same behavior observed in the synthesis of $CsPbBr_3$ QDs,

DOI: 10.1021/acs.chemmater.9b01515
Chem. Mater. 2019, 31, 5655–5662

as will be shown later. These observations indicate that the halide equilibrium plays a key role in determining t of $CsPbBr_3$ NRs and NWs in a similar manner to the isotropic size control of the cube-shaped $CsPbBr_3$ QDs. Compared to the hot-injection synthesis of $CsPbBr_3$ QDs, the range of t control is limited to the smaller length scale ($t \leq 3$ nm) in both NRs and NWs. This is likely due to the lower reaction temperature that limits the applicability of halide equilibrium as the size control mechanism to the thinner structures having a sufficiently low kinetic barrier for Br^- diffusion within the lattice. In fact, the lower kinetic barrier for ion diffusion in the smaller nanocrystals, which can more readily drive the process dictated by the chemical equilibrium, was recognized earlier and utilized in reversible cation exchange at room temperature in other colloidal QDs.[35] When the synthesis of the thicker nanocrystals was attempted by further lowering [Br^-] in the case of NRs, t became less controllable resulting in the mixed t, as will be discussed in detail in Figure 3.

Figure 2 shows the distribution of the thickness (t), width (w), and length (l) of NRs with two different t, determined from the analysis of TEM images. The thickness (t) that determines the PL emission wavelengths (λ_{PL}) via quantum confinement exhibited particularly high size uniformity for t = 2 and 3 nm. The exciton luminescence is centered at λ_{PL} = 432 and 460 nm for t = 2 and 3 nm, respectively, as shown in Figure 1a,b. The number of $PbBr_6^{4-}$ octahedral units (n) along the thickness direction for t = 2 and 3 nm corresponds, respectively, to n = 3 and 5, as can be seen in the highresolution TEM images shown in Figure 1k,l. On the other hand, NRs with the thickness corresponding to n = 4 or other even numbers were not identified as the major species in this study. When the synthesis of the thicker NRs was attempted by further reducing [Br^-], t became larger but less controllable resulting in the mixture of different t, as reflected in the PL spectrum shown in Figure 3a. Interestingly, the fit of the PL spectrum in Figure 3a shows the major peaks at λ_{PL} that corresponds to t with odd-numbered n (e.g., 3, 5, 7) reported in the earlier study.[23] Figure 3b shows several single-particle PL spectra of NRs appearing at the frequently observed regions of λ_{PL}, which are also consistent with the dominance of oddnumbered n in the ensemble of NRs with different t. The

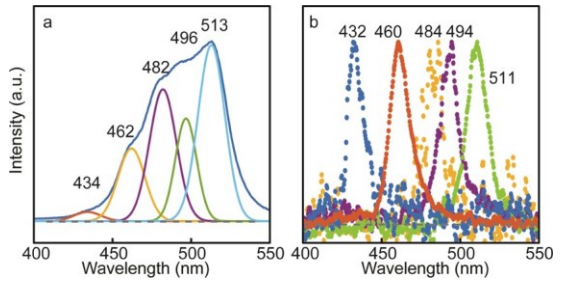

Figure 3. (a) PL spectrum of a heterogeneous ensemble of NRs with different thicknesses. The spectrum was fit to a sum of Gaussian functions centered at 434, 462, 482, 496, and 513 nm. The three peaks at 434, 462, and 482 nm are assigned to n = 3, 5, and 7, respectively. (b) Single-particle PL spectra of NRs chosen from the same ensemble sample shown in (a).

reason for the appearance of t that differ by $\Delta n = 2$ rather than for every possible value of n will be discussed shortly. The distribution of width (w) of NRs shown in Figure 2b was determined from the TEM images of the NRs lying down flat on a TEM grid (insets in Figure 1f,g), which is more frequently observed on the low-particle-density area on the TEM grid. The average w is ~5 nm with the wider distribution (±1.2 nm) than t for both t = 2 and 3 nm NRs. We can readily confirm that ~5 nm measured from the TEM image is not t of the thicker NRs since λ_{PL} determined by the shortest quantumconfined dimension corresponds to only t = 2 or 3 nm. The average length (l) of the NRs is ~35 and ~50 nm for t = 2 and
3 nm, respectively, and exhibits significantly wider distribution than t, as shown in Figure 2c. The longer l for the thicker NRs is likely due to the longer reaction time typically required for the synthesis of the thicker NRs.

NWs are also produced with two well-defined thicknesses at t = 2 and 3 nm corresponding to n = 3 and 5. Similarly to the case of NRs, thinner NWs were formed at the higher [Br^-] condition. Confirmation of the morphology as NWs (t = w) as opposed to NRs (t < w) was made by examining the TEM images with low particle density, which readily reveals the wider w from the particles lying down flat if NRs are present as discussed above. In contrast to NRs, only one size was observed for the shorter dimension regardless of the areal density of the nanocrystals on the TEM grid indicating t = w. Peak positions of the exciton luminescence in NWs are λ_{PL} = 434 and 458 nm for t = 2 and 3 nm, respectively, which are close to those of NRs of the same thickness. The length of NWs grew up to several hundred nm, which generally increases with increasing reaction time (Figure S4). For the

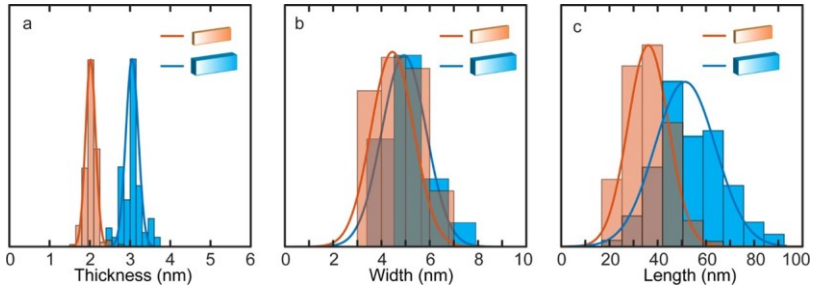

DOI: 10.1021/acs.chemmater.9b01515
Chem. Mater. 2019, 31, 5655−5662

Figure 2. Histograms showing the distribution of thickness (a), width (b), and length (c) of NRs with t = 2 nm (red) and t = 3 nm (blue).

NPLs that required higher [Br^-] than NRs and NWs, the thickness was limited to only t = 2 nm, as shown in Figure 1c,h,m. The lateral shape is approximately square (w ≈ l) in the size range of tens to >100 nm depending on the reaction time (Figure S5). λ_{PL} of NPLs is 434 nm, which is also very close to those of NRs and NWs of the same thickness.

The results above show that the size in different directions (t, w, and l) in NRs, NWs, and NPLs exhibits a different dependence on [Br^-] and the reaction kinetics in a significantly more complex manner than in isotropic QDs synthesized under hot-injection condition. Nevertheless, a valuable insight into the simultaneous involvement of the halide equilibrium and anisotropic growth kinetics in determining the size in different directions is obtained from the in situ photoluminescence (PL) measurement during the reaction. Figure 4a–d shows the false-color contour plots of the time-dependent PL spectra for NRs (a, b) and NWs (c, d)

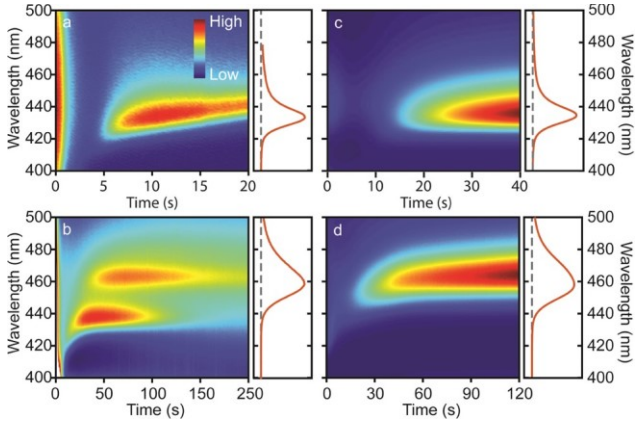

Figure 4. In situ measurement of photoluminescence (PL) during the synthesis of NRs and NWs. (a),(b) NRs with t = 2 and 3 nm, respectively. (c),(d) NWs with t = 2 and 3 nm, respectively. The PL spectra of the final product are shown on the right side of the contour plots.

of two different thicknesses, t = 2 and 3 nm, respectively. The panel on the right side of each contour plot shows the PL spectrum of the final product.

For t = 2 nm NRs shown in Figure 4a, the PL at λ_{PL} = 425 nm appearing at 5 s develops into the terminal PL at λ_{PL} = 432 nm within an additional 10 s, which remains unchanged as the reaction continues. Since it takes ∼5 s for acetone and ODE to form a homogeneous phase and fully release Br^- from its precursor into the reaction mixture (Figure S6), the initial nanocrystal with observable PL was formed almost immediately after Br^- is released. As the reaction continues, the produced NRs begin to precipitate out of the solution at ∼15 s, resulting in the apparent decrease of the intensity and distortion of the PL spectrum from strong self-absorption and scattering of the PL in Figure 4a. For t = 3 nm NRs shown in Figure 4b, PL during the early time (<10 s) is similar to t = 2 nm NRs. Interestingly, a discontinuous jump of λ_{PL} from 432 to 460 nm corresponding to Δn = 2 begins to occur at ∼30 s and continues for several minutes. The discontinuous red shift of λ_{PL} reflecting the abrupt increase of t by Δn = 2 suggests the simultaneous addition of two $PbBr_6^{4-}$ octahedral units along the direction of the thickness, likely adding one on each side of NRs instead of adding one unit after another. This can also explain why the thicknesses of all NRs observed in this study including the heterogeneous ensemble of mixed t shown in Figure 3 differ by Δn = 2, resulting in primarily odd-numbered n instead of all possible n. It is noteworthy that despite the jump of λ_{PL} occurring over a period of ∼100 s in Figure 4b, the terminal λ_{PL} does not change as the reaction continues, further revealing the kinetics-independent characteristics of the equilibrium-based mechanism of determining t. In the case of NWs shown in Figure 4c,d, the initial observable PL appears significantly later than in NRs, presumably due to lower [Br^-] in the reactant mixture resulting in the slower nucleation. As in the case of NRs, Δn between the two NWs shown in Figure 4c,d is 2, and λ_{PL} does not change further with continued reaction once the terminal value is reached. These results indicate that the same mechanism of determining t is operating in both NRs and NWs. However, no abrupt jump of λ_{PL} is observed for t = 3 nm NWs in Figure 4d in contrast to that for NRs. This may indicate that the conversion from n = 3 to 5 occurs more gradually in NWs than in NRs.

The above result clearly shows that t exhibits a similar pattern of the size control to that of $CsPbBr_3$ QDs from hotinjection synthesis, where the size was determined by [Br^-] in the reactant mixture independent of the reaction kinetics at a given reaction temperature. Both NRs and NWs show the higher stoichiometric Br^- composition for the smaller t, as summarized in Table 1, which is necessary to obtain the

Table 1. Stoichiometric Ratio and PL Quantum Yield (Φ_s) of $CsPbBr_3$ NRs and NWs

Sample	Cs/Pb ratio	Br/Pb ratio	Φ_s

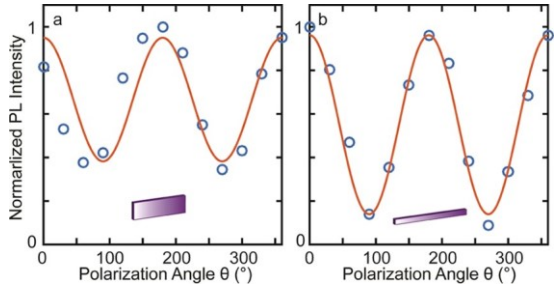

Figure 5. Polarization angle-dependent PL intensity from single $CsPbBr_3$ NR (a) and NW (b) each with t = 3 nm under a fixed polarization angle of the excitation light.

DOI: 10.1021/acs.chemmater.9b01515
Chem. Mater. 2019, 31, 5655−5662

NR, t=2 nm	0.49±0.01	2.9±0.1	0.3±0.05
NR, t=3 nm	0.63±0.01	2.6±0.1	0.4±0.1
NW, t=2 nm	0.45±0.01	4.2±0.2	0.20±0.05
NW, t=3 nm	0.66±0.01	2.8±0.2	0.50±0.05

thinner nanocrystals at higher [Br^-] in the reactant mixture via halide equilibrium. In contrast to t, l is determined in a very different way following the typical pattern of kinetically controlled growth, i.e., increase in size with the reaction time. The different mechanism of determining w under different reaction conditions, which differentiates NRs (w > t), NWs (w = t), and NPLs (w = l), is intriguing and requires further study to obtain deeper understanding. Nevertheless, the simultaneous operation of the equilibrium-based control of t and the kinetic control of l offers a convenient route to introduce high optical anisotropy while maintaining high spectroscopic homogeneity of the confined exciton absorption and emission. Additionally, the colloidal solution of these nanocrystals maintains the strongly confined exciton absorption feature without showing the signature of changing thickness or the formation of other phases under a moderately intense and extended (~3 W/cm^2 at 405 nm for 1 h) photoexcitation condition (Figure S7). The nanocrystals less thoroughly purified by precipitation/resuspension exhibited further growth under the photoexcitation, indicating the importance of removing excess unreacted salts for the stability of these nanocrystals. The purified nanocrystal solutions were stable under an ambient condition for several months (Figure S8).

To characterize the optical anisotropy of NRs and NWs, the emission polarization angle-dependent exciton PL intensity was measured under the linearly polarized excitation employing single-particle spectroscopy, as shown in Figure 5. The detailed description of the measurement is in the Experimental Section. NR and NW show ~60 and ~90% modulation depths in the PL intensity, respectively. NW shows a higher PL anisotropy than NR that may reflect the larger aspect ratio of NW. The high PL anisotropy of NRs and NWs with high quantum yield (Table 1) will be particularly useful for photonic applications benefiting from the directional light emission from the ordered assembly of these nanocrystals.[1,36−39]

As mentioned earlier, $CuBr_2$ is rather unusual as the source of excess Br^- in its ability to release Br^- at a higher concentration than other MBr_2 at room temperature when the reaction is initiated by adding acetone to the reactant mixture. In a separate experiment, we confirmed that Cu^{2+} can form a complex with more than two Br^- ions stably in a nonpolar solvent, especially in the presence of amine ligands, and the formed complex can release Br^- readily in a polar solvent environment. $CsPbBr_3$ nanocrystals in a nonpolar solvent was immediately destroyed when $CuBr_2$ was added with a small amount of oleylamine in contrast to other MBr_2 (e.g., $CoBr_2$, $ZnBr_2$) since Cu^{2+} pulls Br^- from the nanocrystals to form a brown-colored complex. Under the typical hotinjection synthesis condition of $CsPbBr_3$ nanocrystals in a nonpolar solvent, the addition of $CuBr_2$ in the reactant mixture also suppresses the formation of $CsPbBr_3$ nanocrystals because Br^- binds strongly to Cu^{2+}. $CsPbBr_3$ nanocrystals are produced only after increasing the solvent polarity by adding acetone, which releases Br^- from the complex. Although the exact structure of the complex is not fully characterized in our study, $CuBr_4L_2$ (L = R-NH_4) is a possible species that can exist in the reactant mixture.[40] The rapid release of Br^- from Cu^{2+} complex upon the addition of acetone was also confirmed by monitoring the absorption spectrum of the ODE solution of the mixture of $PbBr_2$, $CuBr_2$, OAm, and OA. The initial dark brown color of the solution turned green immediately after ODE, and acetone forms a homogeneous phase and the absorption spectrum stayed the same (Figure S6), which indicates the immediate release of Br^- via replacement of the ligand coordinated on Cu^{2+}. We consider that Cu^{2+} ion′s ability to hold a relatively large amount of Br^- in a nonpolar environment and rapidly release them into a polar environment plays a crucial role in creating NRs and NPLs through the combined action of equilibrium and kinetic anisotropy.

While all anisotropic nanocrystals were obtained by varying only the amount and source of Br^- at fixed room temperature (23 °C) in this study, varying the temperature has a significant impact on the morphology. For instance, the reaction condition that forms NWs using $CoBr_2$ as the source of excess Br^- at room temperature (23 °C) produces NPLs with t = 2 nm when the temperature is increased to 35 °C (Figure S9). The apparent effect of the temperature increase by 12 °C in this example is equivalent to the effect of increasing [Br^-] in the reactant mixture at the same room temperature, likely due to the increased solubility of the metal halide salt. Certainly, varying the temperature alters multiple factors that can affect the morphology and size of the reaction product, which includes not only the effective concentration of the reactants but also the equilibrium and kinetic anisotropy. While we did not explore the two-dimensional parameter space of temperature and [Br^-] simultaneously, the above result suggests the possible expansion of the controllability of the size and anisotropic morphology by exploring the wider range of temperature supporting the anisotropic growth.

Since MBr_2 (M = Cu, Co) is used as the source of excess Br^-, it is important to examine the potential effect of M^{2+}

DOI: 10.1021/acs.chemmater.9b01515
Chem. Mater. 2019, 31, 5655−5662

present in the reactant mixture on the structure and the properties of the final nanocrystal product. One obvious possibility is the substitutional doping of Pb^{2+} with M^{2+}, which has been previously shown to be possible for some metal ions such as Mn^{2+} either under hot-injection condition or under the condition that facilitates cation exchange.[41−43] Elemental analysis shows no incorporation of Co^{2+} beyond its detection limit (2.6×10^{-2} ppb) in the nanocrystals formed using $CoBr_2$ as the source of excess Br^- under the experimental condition employed here. On the other hand, Cu^{2+} was found to be doped in the lattice of $CsPbBr_3$ nanocrystals at a doping concentration of ∼1% or below depending on the amount of $CuBr_2$ used in this study. At this doping level, Cu^{2+} in $CsPbBr_3$ lattice has no undesirable effect on the PL as reflected in the high PL quantum yield (30−40%) of band-edge emission and the absence of any defect emission. On the contrary, we consider that the doping may have enhanced the stability and the PL quantum yield of the nanocrystals similarly to the perovskite nanocrystals doped with other cations.[41,44−47] Presently, the extension of the new method to $CsPbCl_3$ and $CsPbI_3$ anisotropic nanocrystals is partially successful ($CsPbCl_3$ nanorods and $CsPbI_3$ NPLs, Figures S10 and S11). This is due to the much slower reaction kinetics of $CsPbCl_3$ at room temperature and the higher reactivity of CuI_2, requiring the exploration of the wider range of reaction conditions.

CONCLUSIONS

We showed that anisotropic morphology and the size of various one- and two-dimensional anisotropic $CsPbBr_3$ nanocrystals can be controlled by simultaneously utilizing the thermodynamic equilibrium of halide and kinetic anisotropy at the room-temperature reaction. The halide equilibrium-based size control recently shown in the hot-injection synthesis of the isotropic quantum dot was combined with the roomtemperature reaction that promotes the kinetic anisotropy to systematically vary the anisotropic morphology and size. In this approach, only the shortest and strongly quantum-confined dimension of the anisotropic nanocrystals was controlled via halide equilibrium. The size in other directions was determined completely differently following the pattern of a more typical kinetically controlled growth. Systematic variation of the anisotropic morphologies and the size of $CsPbBr_3$ nanocrystals were achieved by varying only the chemical identity and amount of MBr_2 (M = Co, Cu) used as the excess halide source, while all other reaction conditions (e.g., temperature, ligands) were kept the same. Nanoribbons, nanowires, and nanoplatelets produced in this way exhibited a high-ensemble uniformity of optical properties and a well-defined polarization anisotropy of luminescence, which will be important for the future application of anisotropic perovskite nanostructures.

EXPERIMENTAL SECTION

Chemicals. Cesium carbonate (Cs_2CO_3, puratronic, 99.994%, metal basis, Alfa Aesar), lead(II) bromide ($PbBr_2$, puratronic, 99.999% metal basis, Alfa Aesar), copper(II) bromide ($CuBr_2$, 99% metal basis, Alfa Aesar), cobalt(II) bromide ($CoBr_2$, 97%, anhydrous, Alfa Aesar), oleylamine (OAm, technical grade 70%, Sigma-Aldrich), oleic acid (OA, technical grade 90%, Sigma-Aldrich), 1-octadecene (ODE, technical grade 90%, Sigma-Aldrich), acetone (Certified ACS, Fischer), hexane (HPLC grade, Millipore), and methyl acetate (99%, BeanTown Chemical) were used.

Synthesis of Anisotropic $CsPbBr_3$ Nanocrystals. **$CsPbBr_3$ Nanoribbons (NRs).** The precursor solution of Pb and Br was prepared by dissolving $PbBr_2$ (55 mg) and $CuBr_2$ (140 or 300 mg) in a mixture of ODE (5 mL), OA (2 mL), and OAm (2 mL). The precursor solution of Pb and Br was initially degassed at 120 °C under vacuum for 10 min. Subsequently, the precursor solution was heated at 200 °C under a nitrogen atmosphere until all of the metal salts dissolved and cooled down to room temperature. The precursor solution of Cs was prepared by dissolving Cs_2CO_3 (250 mg) in a mixture of ODE (7 mL) and OA (1 mL). The precursor solution of Cs was initially degassed under vacuum and heated at 150 °C under a nitrogen atmosphere until the salt dissolved completely and was kept at >100 °C to prevent solidification of the Cs oleate formed during the process. In a flask containing 9 mL of the precursor solution of Pb and Br at room temperature, 0.4 mL of a Cs precursor solution was added and kept at room temperature. At this stage, the reactant mixture remains unreactive. The reaction that forms NRs was initiated by adding ∼10 mL of acetone in the vial and mixing it vigorously. After 30−250 s of reaction, NRs were separated by centrifugation. The recovered NRs were purified by redispersing in hexane and precipitating again using methyl acetate as the antisolvent. The purified NRs were finally dispersed in hexane for all spectroscopic measurements. A more detailed step-by-step procedure is in the Supporting Information. Different thickness (t) was obtained using different amounts of $CuBr_2$ in the preparation of the precursor solution (t = 2 nm for 300 mg, t = 3 nm for 140 mg of $CuBr_2$).

$CsPbBr_3$ Nanoplatelets (NPLs). All of the procedures are the same as in the synthesis of NRs except the composition of the precursor solution of Pb and Br. $PbBr_2$ (55 mg), $CuBr_2$ (400 mg), and $CoBr_2$ (100 mg) were dissolved in a mixture of ODE (5 mL), OA (2 mL), and OAm (2 mL), which provides higher [Br^-] when the acetone initiates the reaction by liberating Br^- ions from the precursor. A more detailed step-by-step procedure is in the Supporting Information.

$CsPbBr_3$ Nanowires (NWs). The precursor solution of Pb and Br was prepared by dissolving $PbBr_2$ (65 mg) and $CoBr_2$ (20−80 mg) in a mixture of ODE (5 mL), OA (2 mL), and OAm (2 mL) in the same way as in the synthesis of NRs. The precursor solution of Cs used for the synthesis of NWs is the same as in the synthesis of NRs. In a flask, the precursor solution of Cs (0.4 mL) and of Pb and Br (9 mL) at room temperature was mixed together, which remained unreactive. The reaction that forms NWs was initiated by adding ∼10 mL of acetone in the vial and mixing it vigorously. After the reaction completed (40 s for 2 nm NWs and 120 s for 3 nm NWs), NWs were separated by centrifugation and purified in the same way as NRs. A more detailed step-by-step procedure is in the Supporting

DOI: 10.1021/acs.chemmater.9b01515
Chem. Mater. 2019, 31, 5655−5662

Information.

Spectroscopic Characterization. Absorption, photoluminescence quantum yield (PLQY), and photoluminescence (PL) spectra of all $CsPbBr_3$ nanocrystals were made using the fiber-optic-coupled charge-coupled device (CCD) spectrometer (Ocean Optics, USB4000 for absorption and QE65pro for PL). PLQY of the nanocrystal sample (Φ_s) was measured using quinine sulfate in a 0.1 M aqueous sulfuric acid solution exhibiting the PL near 450 nm as the reference with known PLQY of $\Phi_r = 0.54$. Φ_s was calculated from $\Phi_s = \Phi_r(I_s \cdot A_r \cdot n_s^2)/(I_r \cdot A_s \cdot n_r^2)$, where $I_{s(r)}$, $A_{r(s)}$, and $n_{s(r)}$ are the measured integrated PL intensity, absorbance, and refractive index of the reference (r) and nanocrystal sample (s) solutions, respectively. The absorbance of both reference dye and the sample nanocrystals at an excitation wavelength (375 nm) was kept below 0.1 to minimize the effect of reabsorption of the fluorescence in PLQY measurement. The high-speed acquisition mode of a QE65pro spectrometer was used to acquire in situ time-dependent PL spectra during the reaction. A lightemitting diode emitting at 365 nm was used as the excitation source for the PL measurement. The single-particle PL spectra of $CsPbBr_3$ NRs were made using a homebuilt wide-field microscope constructed with an imaging spectrograph (Princeton Instruments, Acton SpectraPro SP-2300) and an electron-multiplying charge-coupled device (EMCCD) (Princeton Instruments, ProEM 16002). Details on the instrument and the single-particle PL measurements are described elsewhere,[33,41] and a brief description of the measurement is below. For each NR sample, a highly diluted colloidal solution was dropcasted onto a thin quartz substrate and placed on top of a quartz prism using index-matching oil to excite the nanocrystals via attenuated total reflection (ATR). The sample was excited at 405 nm with 10 nm bandwidth using a Xe lamp in conjunction with a monochromator (Newport, Oriel Cornerstone 130). The PL from a well-separated single $CsPbBr_3$ nanocrystal collected with the objective (Olympus, PLanFL N 40×) was projected on the narrow slit of the imaging spectrograph using a tube lens (Nikon) and sent to the EMCCD either as an image or as a dispersed spectrum.

Measurement of the PL Polarization Anisotropy. The linear PL polarization anisotropy of the individual $CsPbBr_3$ nanocrystal was measured using the microscope described above, and the same highly diluted nanocrystal sample was drop-casted onto a quartz substrate. Instead of using ATR excitation scheme, the sample was excited from underneath of the quartz substrate using the linearly polarized light from a 405 nm diode laser (Crystalaser). Under the fixed excitation polarization angle, the PL spectrum was recorded as a function of the angle of the polarizer placed between the objective and EMCCD detector.

TEM, X-ray Diffraction, and Elemental Analysis. TEM images were obtained on an FEI Tecnai G2 F20 ST FE-TEM microscope. Powder X-ray diffraction (XRD) data were collected using a BrukerAXS GADDS MWPC diffractometer equipped with Cu Kα X-ray radiation and a multiwire proportional counter. The stoichiometric ratio between Cs and Pb was determined by the elemental analysis performed using inductively coupled plasma mass spectrometry (NexIon 300D). The stoichiometric ratio between Br and Pb was determined by the TEM equipped for energy-dispersive spectroscopy.

ASSOCIATED CONTENT

* Supporting Information

The Supporting Information is available free of charge on the ACS Publications website at DOI: 10.1021/acs.chemmater.9b01515.

Synthesis and purification procedure, XRD patterns, additional TEM and optical spectra, time-dependent absorption spectra of measurement of the precursor solution, and absorption and PL spectra of NPL solution
(PDF)

AUTHOR INFORMATION

Corresponding Author *E-mail: dhson@chem.tamu.edu.

ORCID

Yitong Dong: 0000-0002-7069-3725

Dong Hee Son: 0000-0001-9002-5188

Author Contributions

‖ Y.D. and T.Q. contributed equally to this work.

Notes

The authors declare no competing financial interest.

ACKNOWLEDGMENTS

This research was supported by the Robert A. Welch Foundation A-1639 (Y.D.), NSF CHM-1834568 (T.Q.), and IBS-R026-D1 (D.H.S.). S.J.A. thanks NRF (2011-0030233) for the support during the visit to TAMU. Dr. Nattamai S. P. Bhuvanesh is acknowledged for assistance with XRD measurements.

REFERENCES

(1) Hu, J.; Li, L.-s.; Yang, W.; Manna, L.; Wang, L.-w.; Alivisatos, A. P. Linearly Polarized Emission from Colloidal Semiconductor Quantum Rods. Science 2001, 292, 2060−2063.

(2) Tessier, M. D.; Javaux, C.; Maksimovic, I.; Loriette, V.; Dubertret, B. Spectroscopy of Single CdSe Nanoplatelets. ACS Nano 2012, 6, 6751−6758.

(3) Yan, R.; Gargas, D.; Yang, P. Nanowire photonics. Nat. Photonics 2009, 3, 569.

(4) Wang, J.; Gudiksen, M. S.; Duan, X.; Cui, Y.; Lieber, C. M. Highly Polarized Photoluminescence and Photodetection from Single Indium Phosphide Nanowires. Science 2001, 293, 1455−1457.

DOI: 10.1021/acs.chemmater.9b01515
Chem. Mater. 2019, 31, 5655−5662

(5) Dogan, S.; Bielewicz, T.; Cai, Y.; Klinke, C. Field−effect Transistors Made of Individual Colloidal PbS Nanosheets. Appl. Phys. Lett. 2012, 101, No. 073102.
(6) Huynh, W. U.; Dittmer, J. J.; Alivisatos, A. P. Hybrid NanorodPolymer Solar Cells. Science 2002, 295, 2425−2427.
(7) Hochbaum, A. I.; Yang, P. Semiconductor Nanowires for Energy Conversion. Chem. Rev. 2010, 110, 527−546.
(8) Peng, X.; Manna, L.; Yang, W.; Wickham, J.; Scher, E.; Kadavanich, A.; Alivisatos, A. P. Shape control of CdSe nanocrystals. Nature 2000, 404, 59.
(9) Yu, H.; Li, J.; Loomis, R. A.; Wang, L.-W.; Buhro, W. E. Twoversus three-dimensional quantum confinement in indium phosphide wires and dots. Nat. Mater. 2003, 2, 517.
(10) Manna, L.; Scher, E. C.; Alivisatos, A. P. Synthesis of Soluble and Processable Rod-, Arrow-, Teardrop-, and Tetrapod-Shaped CdSe Nanocrystals. J. Am. Chem. Soc. 2000, 122, 12700−12706.
(11) Schliehe, C.; Juarez, B. H.; Pelletier, M.; Jander, S.; Greshnykh, D.; Nagel, M.; Meyer, A.; Foerster, S.; Kornowski, A.; Klinke, C.; Weller, H. Ultrathin PbS Sheets by Two-Dimensional Oriented Attachment. Science 2010, 329, 550−553.
(12) Ithurria, S.; Tessier, M. D.; Mahler, B.; Lobo, R. P. S. M.; Dubertret, B.; Efros, A. L. Colloidal nanoplatelets with twodimensional electronic structure. Nat. Mater. 2011, 10, 936.
(13) Manna, L.; Milliron, D. J.; Meisel, A.; Scher, E. C.; Alivisatos, A. P. Controlled growth of tetrapod-branched inorganic nanocrystals. Nat. Mater. 2003, 2, 382.
(14) Xia, Y.; Yang, P.; Sun, Y.; Wu, Y.; Mayers, B.; Gates, B.; Yin, Y.; Kim, F.; Yan, H. One-Dimensional Nanostructures: Synthesis, Characterization, and Applications. Adv. Mater. 2003, 15, 353−389.
(15) Trentler, T. J.; Hickman, K. M.; Goel, S. C.; Viano, A. M.; Gibbons, P. C.; Buhro, W. E. Solution-Liquid-Solid Growth of Crystalline III-V Semiconductors: An Analogy to Vapor-Liquid-Solid Growth. Science 1995, 270, 1791−1794.
(16) Yu, H.; Li, J.; Loomis, R. A.; Gibbons, P. C.; Wang; Buhro, W. E. Cadmium Selenide Quantum Wires and the Transition from 3D to 2D Confinement. J. Am. Chem. Soc. 2003, 125, 16168−16169.
(17) Yong, K.-T.; Sahoo, Y.; Choudhury, K. R.; Swihart, M. T.; Minter, J. R.; Prasad, P. N. Shape Control of PbSe Nanocrystals Using Noble Metal Seed Particles. Nano Lett. 2006, 6, 709−714.
(18) Bekenstein, Y.; Koscher, B. A.; Eaton, S. W.; Yang, P.; Alivisatos, A. P. Highly Luminescent Colloidal Nanoplates of Perovskite Cesium Lead Halide and Their Oriented Assemblies. J. Am. Chem. Soc. 2015, 137, 16008−16011.
(19) Zhang, D.; Yu, Y.; Bekenstein, Y.; Wong, A. B.; Alivisatos, A. P.; Yang, P. Ultrathin Colloidal Cesium Lead Halide Perovskite Nanowires. J. Am. Chem. Soc. 2016, 138, 13155−13158.
(20) Pan, A.; He, B.; Fan, X.; Liu, Z.; Urban, J. J.; Alivisatos, A. P.; He, L.; Liu, Y. Insight into the Ligand-Mediated Synthesis of Colloidal $CsPbBr_3$ Perovskite Nanocrystals: The Role of Organic Acid, Base, and Cesium Precursors. ACS Nano 2016, 10, 7943−7954.
(21) Shamsi, J.; Dang, Z.; Bianchini, P.; Canale, C.; Di Stasio, F.; Brescia, R.; Prato, M.; Manna, L. Colloidal Synthesis of Quantum Confined Single Crystal $CsPbBr_3$ Nanosheets with Lateral Size Control up to the Micrometer Range. J. Am. Chem. Soc. 2016, 138, 7240−7243.
(22) Sun, S.; Yuan, D.; Xu, Y.; Wang, A.; Deng, Z. Ligand-Mediated Synthesis of Shape-Controlled Cesium Lead Halide Perovskite Nanocrystals via Reprecipitation Process at Room Temperature. ACS Nano 2016, 10, 3648−3657.
(23) Akkerman, Q. A.; Motti, S. G.; Srimath Kandada, A. R.; Mosconi, E.; D′Innocenzo, V.; Bertoni, G.; Marras, S.; Kamino, B. A.; Miranda, L.; De Angelis, F.; Petrozza, A.; Prato, M.; Manna, L. Solution Synthesis Approach to Colloidal Cesium Lead Halide Perovskite Nanoplatelets with Monolayer-Level Thickness Control. J. Am. Chem. Soc. 2016, 138, 1010−1016.
(24) Amgar, D.; Stern, A.; Rotem, D.; Porath, D.; Etgar, L. Tunable Length and Optical Properties of $CsPbX_3$ (X = Cl, Br, I) Nanowires with a Few Unit Cells. Nano Lett. 2017, 17, 1007−1013.
(25) Imran, M.; Di Stasio, F.; Dang, Z.; Canale, C.; Khan, A. H.; Shamsi, J.; Brescia, R.; Prato, M.; Manna, L. Colloidal Synthesis of Strongly Fluorescent $CsPbBr_3$ Nanowires with Width Tunable down to the Quantum Confinement Regime. Chem. Mater. 2016, 28, 6450− 6454.
(26) Almeida, G.; Goldoni, L.; Akkerman, Q.; Dang, Z.; Khan, A. H.; Marras, S.; Moreels, I.; Manna, L. Role of Acid−Base Equilibria in the Size, Shape, and Phase Control of Cesium Lead Bromide Nanocrystals. ACS Nano 2018, 12, 1704−1711.
(27) Protesescu, L.; Yakunin, S.; Bodnarchuk, M. I.; Krieg, F.; Caputo, R.; Hendon, C. H.; Yang, R. X.; Walsh, A.; Kovalenko, M. V. Nanocrystals of Cesium Lead Halide Perovskites ($CsPbX_3$, X = Cl, Br, and I): Novel Optoelectronic Materials Showing Bright Emission with Wide Color Gamut. Nano Lett. 2015, 15, 3692−3696.
(28) Peng, L.; Dutta, A.; Xie, R.; Yang, W.; Pradhan, N. Dot−Wire− Platelet−Cube: Step Growth and Structural Transformations in $CsPbBr_3$ Perovskite Nanocrystals. ACS Energy Lett. 2018, 3, 2014− 2020.
(29) Sichert, J. A.; Tong, Y.; Mutz, N.; Vollmer, M.; Fischer, S.; Milowska, K. Z.; García Cortadella, R.; Nickel, B.; Cardenas-Daw, C.; Stolarczyk, J. K.; Urban, A. S.; Feldmann, J. Quantum Size Effect in Organometal Halide Perovskite Nanoplatelets. Nano Lett. 2015, 15, 6521−6527.
(30) Aharon, S.; Etgar, L. Two Dimensional Organometal Halide Perovskite Nanorods with Tunable Optical Properties. Nano Lett. 2016, 16, 3230−3235.
(31) Cho, J.; Choi, Y.-H.; O′Loughlin, T. E.; De Jesus, L.; Banerjee, S. Ligand-Mediated Modulation of Layer Thicknesses of Perovskite Methylammonium Lead Bromide Nanoplatelets. Chem. Mater. 2016, 28, 6909−6916.
(32) Levchuk, I.; Osvet, A.; Tang, X.; Brandl, M.; Perea, J. D.; Hoegl, F.; Matt, G. J.; Hock, R.; Batentschuk, M.; Brabec, C. J. Brightly Luminescent and Color-Tunable Formamidinium Lead Halide Perovskite $FAPbX_3$ (X = Cl, Br, I) Colloidal Nanocrystals. Nano Lett. 2017, 17, 2765−2770.
(33) Dong, Y.; Qiao, T.; Kim, D.; Parobek, D.; Rossi, D.; Son, D. H. Precise Control of Quantum Confinement in Cesium Lead Halide Perovskite Quantum Dots via Thermodynamic Equilibrium. Nano Lett. 2018, 3716−3722.
(34) Parobek, D.; Dong, Y.; Qiao, T.; Son, D. H. Direct HotInjection Synthesis of Mn-Doped $CsPbBr_3$ Nanocrystals. Chem. Mater. 2018, 30, 2939−2944.
(35) Son, D. H.; Hughes, S. M.; Yin, Y.; Paul Alivisatos, A. Cation Exchange Reactions in Ionic Nanocrystals. Science 2004, 306, 1009− 1012.
(36) Gudiksen, M. S.; Lauhon, L. J.; Wang, J.; Smith, D. C.; Lieber, C. M. Growth of Nanowire Superlattice Structures for Nanoscale Photonics and Electronics. Nature 2002, 415, 617.
(37) Zhu, H.; Fu, Y.; Meng, F.; Wu, X.; Gong, Z.; Ding, Q.; Gustafsson, M. V.; Trinh, M. T.; Jin, S.; Zhu, X. Y. Lead halide

DOI: 10.1021/acs.chemmater.9b01515
Chem. Mater. 2019, 31, 5655−5662

perovskite nanowire lasers with low lasing thresholds and high quality factors. Nat. Mater. 2015, 14, 636.

(38) Shi, Z.-F.; Li, Y.; Li, S.; Ji, H.-F.; Lei, L.-Z.; Wu, D.; Xu, T.-T.; Xu, J.-M.; Tian, Y.-T.; Li, X.-J. Polarized emission effect realized in $CH_3NH_3PbI_3$ perovskite nanocrystals. J. Mater. Chem. C 2017, 5, 8699−8706.

(39) Liu, L.; Huang, S.; Pan, L.; Shi, L.-J.; Zou, B.; Deng, L.; Zhong, H. Colloidal Synthesis of $CH_3NH_3PbBr_3$ Nanoplatelets with Polarized Emission through Self-Organization. Angew. Chem. Int. Ed. 2017, 56, 1780−1783.

(40) Kosower, E. M.; Martin, R. L.; Meloche, V. W. Copper(II) Bromide Complexes. J. Am. Chem. Soc. 1957, 79, 1509−1510.

(41) Parobek, D.; Roman, B. J.; Dong, Y.; Jin, H.; Lee, E.; Sheldon, M.; Son, D. H. Exciton-to-Dopant Energy Transfer in Mn-Doped Cesium Lead Halide Perovskite Nanocrystals. Nano Lett. 2016, 16, 7376−7380.

(42) Liu, W.; Lin, Q.; Li, H.; Wu, K.; Robel, I.; Pietryga, J. M.; Klimov, V. I. Mn^{2+}-Doped Lead Halide Perovskite Nanocrystals with Dual-Color Emission Controlled by Halide Content. J. Am. Chem. Soc. 2016, 138, 14954−14961.

(43) van der Stam, W.; Geuchies, J. J.; Altantzis, T.; van den Bos, K. H. W.; Meeldijk, J. D.; Van Aert, S.; Bals, S.; Vanmaekelbergh, D.; de Mello Donega, C. Highly Emissive Divalent-Ion-Doped Colloidal $CsPb_{1-x}M_xBr_3$ Perovskite Nanocrystals through Cation Exchange. J. Am. Chem. Soc. 2017, 139, 4087−4097.

(44) Akkerman, Q. A.; Meggiolaro, D.; Dang, Z.; De Angelis, F.; Manna, L. Fluorescent Alloy $CsPb_xMn_{1-x}I_3$ Perovskite Nanocrystals with High Structural and Optical Stability. ACS Energy Lett. 2017, 2, 2183−2186.

(45) Yong, Z.-J.; Guo, S.-Q.; Ma, J.-P.; Zhang, J.-Y.; Li, Z.-Y.; Chen, Y.-M.; Zhang, B.-B.; Zhou, Y.; Shu, J.; Gu, J.-L.; Zheng, L.-R.; Bakr, O. M.; Sun, H.-T. Doping-Enhanced Short-Range Order of Perovskite Nanocrystals for Near-Unity Violet Luminescence Quantum Yield. J. Am. Chem. Soc. 2018, 140, 9942−9951.

(46) Abdelhady, A. L.; Saidaminov, M. I.; Murali, B.; Adinolfi, V.;
Voznyy, O.; Katsiev, K.; Alarousu, E.; Comin, R.; Dursun, I.; Sinatra, L.; Sargent, E. H.; Mohammed, O. F.; Bakr, O. M. Heterovalent Dopant Incorporation for Bandgap and Type Engineering of Perovskite Crystals. J. Phys. Chem. Lett. 2016, 7, 295−301.

(47) Begum, R.; Parida, M. R.; Abdelhady, A. L.; Murali, B.; Alyami, N. M.; Ahmed, G. H.; Hedhili, M. N.; Bakr, O. M.; Mohammed, O. F. Engineering Interfacial Charge Transfer in $CsPbBr_3$ Perovskite Nanocrystals by Heterovalent Doping. J. Am. Chem. Soc. 2017, 139, 731−737.

DOI: 10.1021/acs.chemmater.9b01515
Chem. Mater. 2019, 31, 5655−5662